Dalton Transactions

ROYAL SOCIETY OF CHEMISTRY

PAPER

View Article Online
View Journal | View Issue

Cite this: *Dalton Trans.*, 2020, **49**, 4425

Structural, magnetic, redox and theoretical characterization of seven-coordinate first-row transition metal complexes with a macrocyclic ligand containing two benzimidazolyl *N*-pendant arms†

Bohuslav Drahoš, *[a] Ivana Císařová, [b] Oleksii Laguta, [c] Vinicius T. Santana, [c] Petr Neugebauer [c] and Radovan Herchel [a]

A structurally new heptadentate derivative of a 15-membered pyridine-based macrocycle containing two benzimidazol-2-yl-methyl *N*-pendant arms (**L** = 3,12-bis((1*H*-benzimidazol-2-yl)methyl)-6,9-dioxa-3,12,18-triazabicyclo[12.3.1]octadeca-1(18),14,16-triene) was synthesized and its complexes with the general formula $[M(\mathbf{L})](ClO_4)_2{\cdot}1.5CH_3NO_2$ (M = Mn^{II} (**1**), Fe^{II} (**2**), Co^{II} (**3**) and Ni^{II} (**4**)) were thoroughly investigated. X-ray crystal structures confirmed that all complexes are seven-coordinate with axially compressed pentagonal bipyramidal geometry having the largest distortion for Ni^{II} complex **4**. Fe^{II}, Co^{II} and Ni^{II} complexes **2**, **3** and **4** show rather large magnetic anisotropy manifested by moderate to high obtained values of the axial zero-field splitting parameter *D* (7.9, 40.3, and –17.2 cm^{-1}, respectively). Magneto-structural correlation of the Fe^{II}, Co^{II} and Ni^{II} complexes with **L** and with previously studied structurally similar ligands revealed a significant impact of the functional group in pendant arms on the magnetic anisotropy especially that of the Co^{II} and Ni^{II} complexes and some recommendations concerning the ligand-field design important for anisotropy tuning in future. Furthermore, complex **3** showed field-induced single-molecule magnet behavior described with the Raman (C = 507 K^{-n} s^{-1} for n = 2.58) relaxation process. The magnetic properties of the studied complexes were supported by theoretical calculations, which very well correspond with the experimental data of magnetic anisotropy. Electrochemical measurements revealed high positive redox potentials for $M^{3+/2+}$ couples and high negative redox potentials for $M^{2+/+}$ couples, which indicate the stabilization of the oxidation state +II expected for the σ-donor/π-acceptor ability of benzimidazole functional groups.

Received 15th January 2020,
Accepted 13th February 2020

DOI: 10.1039/d0dt00166j

rsc.li/dalton

Introduction

In the last decade, increased attention has been devoted to the seven-coordinate pentagonal bipyramidal complexes of transition metals[1] and lanthanides[2–6] due to their interesting magnetic properties, which was demonstrated in an increasing number of published articles and reviews concerning this topic.[7–9] These seven-coordinate pentagonal bipyramidal complexes especially of Fe^{II},[10–16] Co^{II},[12,17–22] and Ni^{II},[12,17,23] and more recently also 4d/5d metals like $Mo^{IV/III}$ [24,25] possess large magnetic anisotropy, which is commonly expressed in terms of axial and rhombic zero-field splitting (ZFS) parameters *D* and *E* for transition metal complexes.[26] Due to their large axial magnetic anisotropy, they have been successfully employed in the construction of single-molecule magnets (SMMs).[27,28] SMMs are compounds showing slow relaxation of magnetization based on pure molecular origin (no long range ordering typical of bulk magnets) and therefore they behave as "nanomagnets" which could find many applications in different fields of interest, *e.g.* in high-density storage media, spintronics, quantum computing *etc.*[29] Unfortunately, SMMs operate

[a]*Department of Inorganic Chemistry, Faculty of Science, Palacký University, 17. listopadu 12, 771 46 Olomouc, Czech Republic. E-mail: bohuslav.drahos@upol.cz; Fax: +420585 634 954; Tel: +420 585 634 429*
[b]*Department of Inorganic Chemistry, Faculty of Science, Charles University, Hlavova 2030, 128 00 Prague, Czech Republic*
[c]*Central European Institute of Technology, CEITEC BUT, Purkyňova 656/123, 61200 Brno, Czech Republic*

† Electronic supplementary information (ESI) available: IR and MS spectra of the ligand and studied complexes, 2D NMR spectra of the ligand **L**, HFEPR data, additional magnetic data and cyclic voltammograms, crystal data and structure refinements, results of continuous shape measures, parameters of one-component Debye model. CCDC 1942109–1942112. For ESI and crystallographic data in CIF or other electronic format see DOI: 10.1039/D0DT00166J

at very low temperature. The greatest progress has been achieved for dysprosium metallocenes with a blocking temperature of 60 K,[30] and the current record breaking the liquid nitrogen temperature is 80 K.[31] In order to increase this temperature, it is necessary to (i) increase the energy of magnetic moment reversal (U_{eff}), which is defined for transition metal complexes as $U_{eff} = |D|S^2$ or $U_{eff} = |D|(S^2 - \frac{1}{4})$ for the integer or non-integer ground spin state, S,[27,28] while for lanthanides with inner shell 4f electrons, large unquenched orbital moments and strong spin–orbit coupling (total momentum J is used) it is based on strong single-ion anisotropy and cannot be described in terms of ZFS spin Hamiltonian parameters, and to (ii) slow down the relaxation of magnetization by understanding all potential relaxation mechanisms including Orbach, direct and Raman mechanisms or quantum tunneling, and by their consequent elimination. Nevertheless, because the relaxation processes are rather complex, the approach (ii) is quite complicated and despite some first attempts,[32] still many questions remain unclear in this field. On the other hand, it was found that for high U_{eff}, not the total spin (S) of the magnetic ground state, but the axial magnetic anisotropy (D) is in fact the key parameter, which has to be tuned and enlarged in order to construct more efficient SMMs.

Such tuning can be achieved by modification of the coordination environment of the metal centre, *i.e.* rational ligand design. In the case of pentagonal bipyramidal complexes, two strategies have been successfully employed previously. In the first one, a pentadentate acyclic (**L4**,[11,22,33] **L5**)[19] or macrocyclic ligand (**L1**, Fig. 1)[21,34] is coordinated in the equatorial plane (these ligands differ in donor atoms, rigidity, electron distribution, and cavity size) while two apical monodentate co-ligands (varying in σ-donor/π-acceptor properties) are exchanged. The second strategy is based on the structural modification of the pentadentate macrocyclic ligand (*e.g.* **L1** or 1,10-diaza-15-crown-5)[35,36] with two pendant arms containing various functional groups with different coordination abilities (2-pyridylmethyl in **L2**,[12,37] acetate in **L3**,[38] 2-aminobenzyl in **L6**[35] and 2-benzimidazolylmethyl in **L7**, Fig. 1).[36] A significant influence on the magnetic anisotropy of the $Fe^{II/III}$, Co^{II} and Ni^{II} complexes with **L2**[12] and **L3**[38] has been observed (Fig. 1), but unfortunately, no clear trend could be elucidated because of the very complex description of the bond character in the complexes and various contradictory structural parameters.

In order to further investigate the effect of different functional groups in pendant arms and to obtain any reasonable magneto-structural correlation,[39] the macrocyclic ligand **L1** has been modified with two 2-benzimidazolylmethyl pendant arms to give a structurally new ligand, **L** (Fig. 1). In fact, benzimidazolyl groups can act as better σ-donors in comparison with pyridine moieties[40,41] and thus, they could provide a stronger axial ligand field, which according to the theoretical

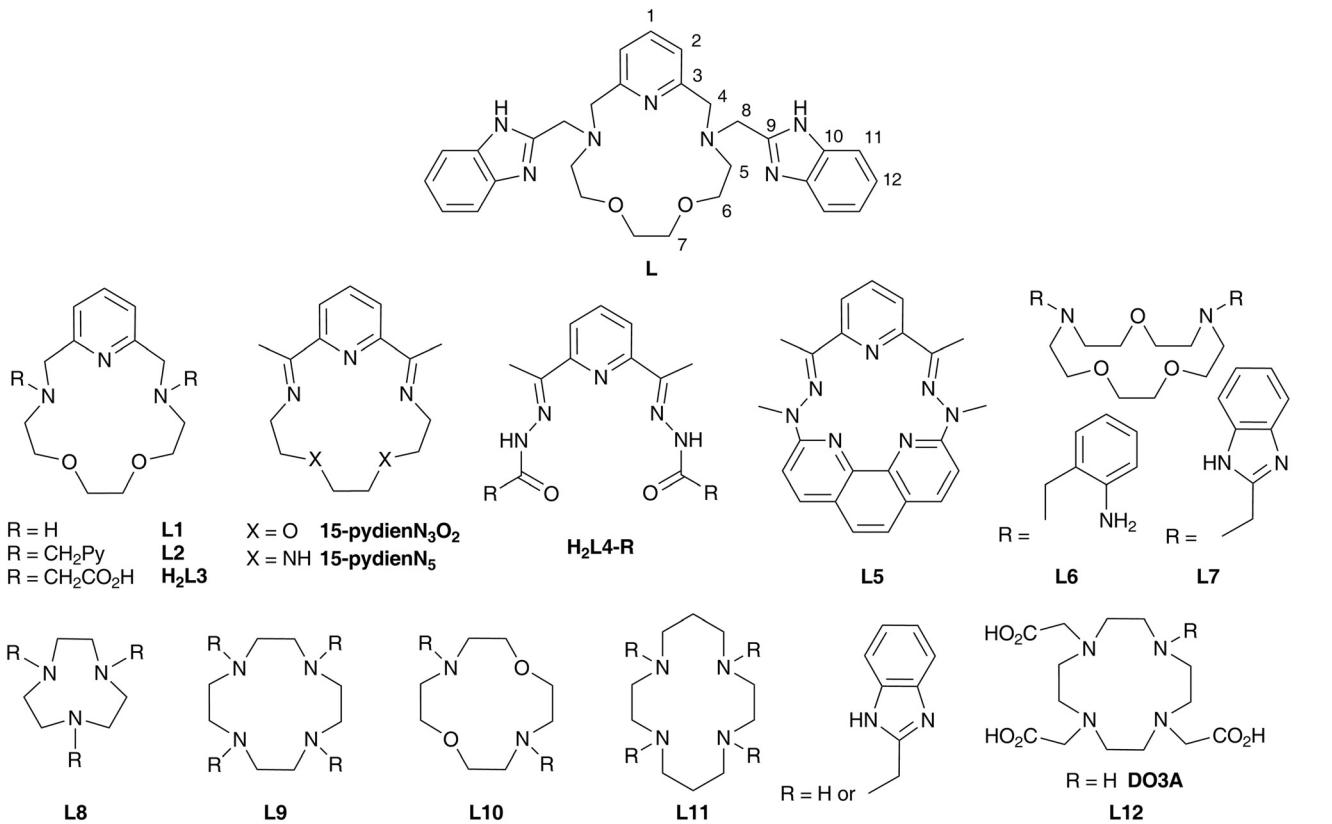

Fig. 1 Structural formulas of studied ligand L together with its atom numbering (applied for assignment of NMR signals) and ligands discussed in the text.

predictions[17] could beneficially influence the magnetic anisotropy especially in the case of pentagonal bipyramidal Fe^{II} and Ni^{II} complexes.[17] Moreover, this ligand is a new member of a relatively small family of rarely documented macrocycles modified with benzimidazolyl pendant arms (Fig. 1, **L7**,[36] differently-substituted triazacyclononanes **L8**,[42,43] tetraazacyclododecanes (cyclenes) **L9**,[44,45] its dioxa-derivative **L10**,[46] tetraazacyclotetradecanes (cyclames) **L11**[47] and its DO3A derivative **L12**).[48]

Thus, in this paper, a structurally new ligand, **L**, has been synthesized and its Mn^{II}, Fe^{II}, Co^{II} and Ni^{II} complexes have been prepared and studied in detail. Their structural, magnetic and redox properties were thoroughly investigated and compared with those of previously studied systems containing ligands **L2** and **L3**. The obtained results were supported by extensive theoretical calculations.

Experimental section

Materials and methods

Ligand **L1**[12,49] and 2-chloromethylbenzimidazole[50] were synthesized according to the literature procedures. All the solvents (VWR International, Fontenay-sous-Blois, France) and other chemicals were purchased from commercial sources (Acros Organics, Geel, Belgium and Sigma-Aldrich, St. Louis, MO, USA) and used as received.

Elemental analysis (C, H, N) was performed using a Flash 2000 CHNO-S analyzer (Thermo Scientific, Waltham, MA, USA). The mass spectra (Fig. S1†) were collected using an LCQ Fleet mass spectrometer (Thermo Scientific, Waltham, MA, USA) equipped with an electro spray ion source and a three-dimensional (3D) ion-trap detector in the positive/negative mode. The infrared (IR) spectra of the ligand and the studied complexes (Fig. S2†) were recorded using a Thermo Nicolet NEXUS 670 FT-IR spectrometer (Thermo Nicolet, Waltham, MA, USA) or a Jasco FT/IR-4700 spectrometer (Jasco, Easton, MD, USA) using the ATR technique on a diamond plate in the range of 400–4000 cm^{-1}. ^1H and ^{13}C NMR spectra were recorded using a 400-MR NMR spectrometer (Varian, Palo Alto, CA, USA) at 25 °C: ^1H 399.95 MHz, chloroform-*d* ($CDCl_3$, tetramethylsilane) δ = 0.00 ppm, and ^{13}C 100.60 MHz, ($CDCl_3$, residual solvent peak) δ = 77.0 ppm. The multiplicity of the signals is indicated as follows: s – singlet, d – doublet, t – triplet, m – multiplet, and bs – broad singlet. Deuterated solvent $CDCl_3$ containing 0.03% of TMS purchased from Sigma Aldrich was used as received. The atom numbering scheme used for NMR data interpretation is shown in Fig. 1. The carbon and hydrogen atoms were assigned according to the spectra obtained from two-dimensional correlation experiments ^1H–^1H gs-COSY, ^1H–^{13}C gs-HMQC and ^1H–^{13}C gs-HMBS (see Fig. S3 and S4†). The temperature dependence of the magnetization at B = 0.1 T from 1.9 to 300 K and the isothermal magnetization at T = 2, 5, and 10 K up to B = 9 T were measured using PPMS Dynacool with the VSM module (Quantum Design Inc., San Diego, CA, USA). The experimental data were corrected for diamagnetism and the signal of the sample holder. Dynamic magnetic properties were studied by measuring AC susceptibility using an MPMS XL7 SQUID magnetometer (Quantum Design Inc., San Diego, CA, USA). High frequency/field electron paramagnetic resonance spectroscopy (HFEPR) was performed at CEITEC (Brno, CZ) using a home-built spectrometer equipped with a cryogen-free 16 T superconducting magnet (Cryogenics Ltd, London, UK), a microwave source for measurements from 90 GHz to 500 GHz (Virginia Diodes Inc., Charlottesville, VA, USA), and quasi-optical components in the same range (Thomas Keating Ltd, Billingshurst, UK). The samples were milled with 20% eicosane and made into a ∅5 mm pellet to be placed inside the sample holder for induction mode HFEPR with a modulation frequency of 10 kHz and an amplitude of 0.4 mT. The spectra were obtained at 4 K and 15 K. Simulations were performed using EasySpin[51] in MATLAB.[52] Cyclic voltammetry was measured using an electrochemical analyzer CHI600C (CH Instrument Inc., Austin, TX, USA). A conventional electrochemical three-electrode-type cell with a Ag/Ag^+ reference electrode (0.01 M $AgNO_3$ in 0.1 M TBAP), a platinum wire auxiliary electrode and a glassy carbon working electrode was used during the measurements with a scan rate of 100 mV s^{-1}. The internal ferrocene/ferrocenium standard ($E_{1/2}$ = 0.452/0.478 V *vs.* our Ag/Ag^+ electrode, $E_{1/2}$ = 0.624 V *vs.* SHE)[53] was employed in order to obtain the final potential values referred to SHE. The measurements were performed under an inert argon atmosphere in acetonitrile solution containing tetrabutylammonium perchlorate (TBAP) as a supporting electrolyte (0.1 M) and an appropriate complex (2×10^{-3} M).

Crystal data

Single crystals of studied complexes **1–4** suitable for X-ray structure analysis were prepared as described in the experimental section. X-ray diffraction data were collected using a Nonius Kappa CCD diffractometer equipped with a Bruker APEX-II CCD detector with monochromatized MoKα radiation (λ = 0.71073 Å) at a temperature of 150(2) K. The molecular structures of the studied complexes were solved by direct methods and refined by full matrix least squares based on F^2 (SHELXL 2014/07).[54] The hydrogen atoms on carbon atoms were fixed in idealized positions (riding model) and assigned temperature factors either $H_{iso}(H) = 1.2U_{eq}$(pivot atom) or $H_{iso}(H) = 1.5U_{eq}$ (pivot atom) for the methyl moiety. The hydrogen atoms of the H–N moieties were found using a difference electron density map and refined as riding on the corresponding pivot atom. All four crystals were isostructural, differing mostly in their quality with regard to the degree of disorder of perchlorate anions and solvated nitromethane molecules. One of the nitromethanes is situated near the inversion center of the $P\bar{1}$ space group and is disordered over four positions at least. To improve the precision of an important part of the structures, PLATON[55]/SQUEEZE procedures were applied to correct the diffraction data for its contribution to all structures. The molecular and crystal structures of the

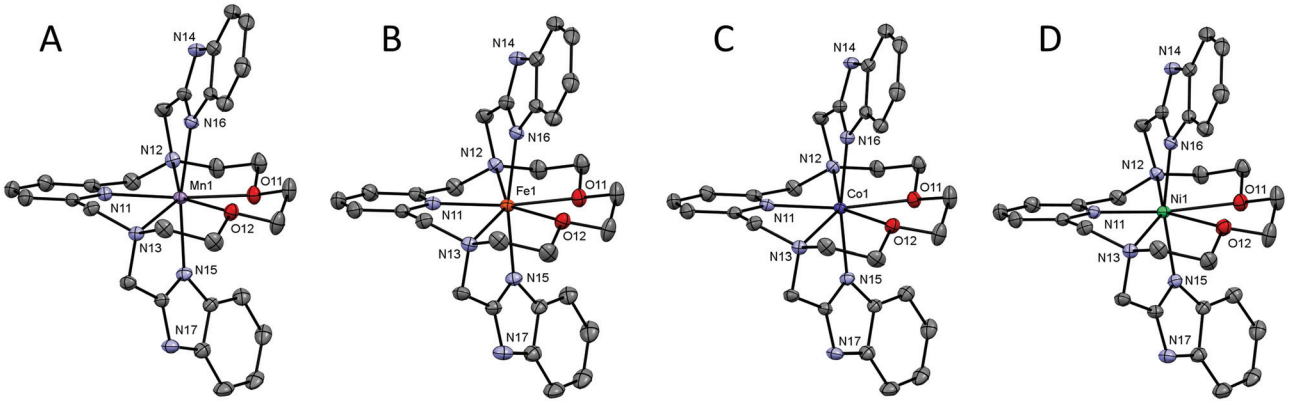

Fig. 2 The molecular structures of the $[ML]^{2+}$ cation in complex **1** (M = Mn^{II}, A), complex **2** (M = Fe^{II}, B), **3** (M = Co^{II}, C) and **4** (M = Ni^{II}, D). Non-hydrogen atoms are drawn as thermal ellipsoids at the 50% probability level. Hydrogen atoms and anions were omitted for clarity. Only one of the two crystallographically independent molecules present in the asymmetric unit of each complex is shown for clarity.

studied complexes, depicted in Fig. 2 and 4 were drawn using the Mercury software.[56]

Syntheses

3,12-Bis((1*H*-benzimidazol-2-yl)methyl)-6,9-dioxa-3,12,18-triazabicyclo[12.3.1]octadeca-1(18),14,16-triene (L). Ligand **L1** (0.50 g, 1.99 mmol), 2-chloromethylbenzimidazole (0.70 g, 4.20 mmol, 2.1 equiv.), K_2CO_3 (2.74 g, 19.9 mmol, 10 equiv.) and NaI (0.30 g, 1.99 mmol) were suspended in 60 mL of CH_3CN and refluxed for 12 h. The hot suspension was filtered through a glass frit and the filtrate was evaporated under reduced pressure to give 1.16 g of yellow solid foam. This solid was redissolved in 50 mL $CHCl_3$, and the obtained solution was extracted three times with 50 mL of deionized water, dried with anhydrous Na_2SO_4, filtered through a glass frit and evaporated under reduced pressure. The product was obtained in the form of pale yellow foam (0.84 g, 82.3%).

MS *m*/*z* (+): 512.24 ($[\mathbf{L} + H^+]^+$, calcd 512.28), 534.29 ($[\mathbf{L} + Na^+]^+$, calcd 534.26), 550.22 ($[\mathbf{L} + K^+]^+$, calcd 550.23).

^{1}H NMR($CDCl_3$): δ 3.19 (H5, t, $^3J_{HH}$ = 4.9 Hz, 4H), 3.41 (H7, s, 4H), 3.50 (H6, t, $^3J_{HH}$ = 4.9 Hz, 4H), 3.94 (H4, s, 4H), 4.04 (H8, s, 4H), 6.93 (H2, d, $^3J_{HH}$ = 7.8 Hz, 2H), 7.14 (H12, m, 4H), 7.39 (H1, t, $^3J_{HH}$ = 7.8 Hz, 1H), 7.48 (H11, m, 2H), 7.60 (H11, m, 2H), 11.55 (NH, bs, 2H)

$^{13}C\{^1H\}$ NMR ($CDCl_3$): δ 53.75 (C8), 57.76 (C5), 62.85 (C4), 68.41 (C6), 69.79 (C7), 111.26 (C11), 118.66 (C11), 121.39 (C12), 121.82 (C2), 121.90 (C12), 133.77 (C10), 136.92 (C1), 143.96 (C10), 155.34 (C9), 158.50 (C3).

General procedure for the preparation of complexes 1–4

Ligand **L** (100 mg, 0.195 mmol) and an appropriate amount of $M(ClO_4)_2{\cdot}6H_2O$ (0.186 mmol, 67 mg of $Mn(ClO_4)_2{\cdot}6H_2O$ and $Fe(ClO_4)_2{\cdot}6H_2O$ or 68 mg of $Co(ClO_4)_2{\cdot}6H_2O$ and $Ni(ClO_4)_2{\cdot}6H_2O$) were dissolved in 4 mL of CH_3OH and left to diethyl ether vapor diffusion at 5 °C. After several days, the well-shaped crystals of the complex formed, were isolated by filtration and redissolved in 1 mL of CH_3NO_2. The obtained solution was filtered *via* a Millipore syringe filter (0.45 μm). The diffusion of diethyl ether vapors into the filtrate at 5 °C resulted in the formation of well-shaped crystals, which were filtered off and dried in air at room temperature. These crystals were also suitable for X-ray diffraction analysis.

Caution! Although we have experienced no difficulties, perchlorate salts of metal complexes with organic ligands are potentially explosive and should be handled with great care even in small quantities.

$[Mn\mathbf{L}](ClO_4)_2{\cdot}1.5CH_3NO_2$ (**1**)

The product was isolated in the form of light yellow crystals (84 mg, 52.7%).

MS *m*/*z* (+): 565.11 ($[Mn(\mathbf{L} - H^+)]^+$, calcd 565.20), 664.89 ($[Mn\mathbf{L} + (ClO_4)^-]^+$, calcd 665.16).

MS *m*/*z* (−): 864.24 ($[Mn\mathbf{L} + 3 \times (ClO_4)^-]^-$, calcd 863.05), 1628.86 ($[2 \times (Mn\mathbf{L}) + 5 \times (ClO_4)^-]^-$, calcd 1629.15).

Anal. calcd (%) for $[Mn\mathbf{L}](ClO_4)_2{\cdot}1.5CH_3NO_2$ ($C_{30.5}H_{37.5}Cl_2MnN_{8.5}O_{13}$, M_r = 857.02): C, 42.74; H, 4.41; N, 13.89. Found C, 43.12; H, 4.58; N, 13.80.

$[Fe\mathbf{L}](ClO_4)_2{\cdot}1.5CH_3NO_2$ (**2**)

The product was isolated in the form of green-brown crystals (61 mg, yield 38.2%).

MS *m*/*z* (+): 566.09 ($[Fe(\mathbf{L} - H^+)]^+$, calcd 566.20), 665.84 ($[Fe\mathbf{L} + (ClO_4)^-]^+$, calcd 666.15).

MS *m*/*z* (−): 865.02 ($[Fe\mathbf{L} + 3 \times (ClO_4)^-]^-$, calcd 864.05), 1631.01 ($[2 \times (Fe\mathbf{L}) + 5 \times (ClO_4)^-]^-$, calcd 1631.15).

Anal. calcd (%) for $[Fe\mathbf{L}](ClO_4)_2{\cdot}1.5CH_3NO_2$ ($C_{30.5}H_{37.5}Cl_2FeN_{8.5}O_{13}$, M_r = 857.92): C, 42.70; H, 4.41; N, 13.88. Found C, 42.22; H, 4.25; N, 13.40.

$[Co\mathbf{L}](ClO_4)_2{\cdot}1.5CH_3NO_2$ (**3**)

The product was isolated in the form of pink crystals (98 mg, yield 61.2%).

MS *m*/*z* (+): 569.12 ($[Co(\mathbf{L} - H^+)]^+$, calcd 569.19), 668.83 ($[Co\mathbf{L} + (ClO_4)^-]^+$, calcd 669.15).

MS *m*/*z* (−): 869.27 ($[Co\mathbf{L} + 3 \times (ClO_4)^-]^-$, calcd 869.05), 1637.11 ($[2 \times (Co\mathbf{L}) + 5 \times (ClO_4)^-]^-$, calcd 1637.15).

Anal. calcd (%) for $[Co\mathbf{L}](ClO_4)_2{\cdot}1.5CH_3NO_2$ ($C_{30.5}H_{37.5}Cl_2CoN_{8.5}O_{13}$, M_r = 861.01): C, 42.55; H, 4.39; N, 13.83. Found C, 42.65; H, 4.32; N, 13.52.

$[NiL](ClO_4)_2{\cdot}1.5CH_3NO_2$ (**4**)

The product was isolated in the form of green crystals (65 mg, yield 40.6%).

MS *m*/*z* (+): 568.17 ($[Ni(L - H^+)]^+$, calcd 568.20), 667.78 ($[NiL + (ClO_4)^-]^+$, calcd 668.15).

MS *m*/*z* (−): 868.62 ($[NiL + 3 \times (ClO_4)^-]^-$, calcd 868.05), 1637.42 ($[2 \times (NiL) + 5 \times (ClO_4)^-]^-$, calcd 1635.15).

Anal. calcd (%) for $[NiL](ClO_4)_2{\cdot}1.5CH_3NO_2$ ($C_{30.5}H_{37.5}Cl_2N_{8.5}NiO_{13}$, M_r = 860.77): C, 42.56; H, 4.39; N, 13.83. Found C, 42.30; H, 4.52; N, 13.72.

Theoretical methods

The ORCA 4.1 computational package was used for quantum chemical calculations.[57,58] The calculations of ZFS parameters were done using state average complete active space self-consistent field (SA-CASSCF)[59] wave functions complemented by the *N*-electron valence second-order perturbation theory (NEVPT2)[60–62] using triple-ζ basis set def2-TZVP[63] for all atoms. Using the state-averaged approach, all multiplets for a given electron configuration were equally weighted. The ZFS parameters, based on dominant spin–orbit coupling contributions from the excited states, were calculated through the quasi-degenerate perturbation theory (QDPT),[64] in which an approximation to the Breit-Pauli form of the spin–orbit coupling operator (SOMF approximation)[65] and the effective Hamiltonian theory[66] were utilized. The calculations utilized the RIJCOSX approximation with the auxiliary basis sets def2/J[67] and def2-TZVP/C.[68] Increased integration grids (Grid5 and GridX5 in ORCA convention) and tight SCF convergence criteria were used in all calculations. Moreover, the recently introduced dynamic correlation dressed CAS with the second-order treatment (DCD-CAS(2)) was also utilized to calculate the ZFS parameters, where the spin–orbit and the spin–spin interactions were included.[69] VESTA 3 program was used to visualize the results of the calculations.[70]

Results and discussion

Syntheses and general characterizations

Ligand **L** was prepared by a common S_N2 substitution reaction of parent macrocycle **L1** and 2-chloromethylbenzimidazole in CH_3CN with K_2CO_3 as a base. Synthesis of all studied complexes was simply based on mixing **L** with the perchlorate of the appropriate metal ion in CH_3OH. The products in the crystalline form obtained after diethyl ether vapor diffusion at 5° C were sensitive to loose co-crystallized CH_3OH solvent molecule(s) and therefore they were re-crystallized from CH_3NO_2. The obtained complexes with the co-crystallized CH_3NO_2 molecules were stable in air and were thoroughly characterized by elemental analysis, mass spectrometry (Fig. S1†) and IR spectroscopy. The measured IR spectra of studied complexes **1–4** are displayed in Fig. S2† and they are identical, which is in accordance with their similar composition and isostructurality (see later). The spectral pattern of all studied complexes **1–4** contains vibrations of the perchlorate anion at 1070 cm^{-1}, stretching C=C and C=N aromatic vibrations at ~1450 cm^{-1}, vibrations of $MeNO_2$ at 1550 cm^{-1}, aliphatic CH stretching vibrations at 2880, 2920 and 3090 cm^{-1}, and NH stretching vibrations at 3250 cm^{-1}.

Crystal structure analysis

The molecular structures of the complex cations of all studied complexes **1–4** are shown in Fig. 2 and crystal data and structure refinements for studied complexes **1–4** can be found in Table S1 in the ESI.† All complexes **1–4** are isostructural, they all crystallized in the triclinic $P\bar{1}$ space group and their molecular structures have a similar structural pattern. The macrocyclic part of the ligand is coordinated in the pentagonal equatorial plane, while the two benzimidazolyl pendant arms are coordinated in apical positions. Thus, all the central atoms are seven-coordinate with pentagonal bipyramidal geometry and a N_5O_2 donor atom set.

A comparison of the M-donor atom distances is shown in Fig. 3, listed in Table 1, and indicates several trends. The $M–N_{(benzimidazole)}$ distances are comparable to those of $M–N_{py}$ and are much shorter than other bonds in the equatorial pentagonal plane, and thus, the pentagonal bipyramid can be considered as slightly axially compressed. Furthermore, in the order going from Mn^{II} to Ni^{II} complex **1** → **4** all M–N distances decrease, which is in agreement with the decreasing ionic radius of complexed metal ions. On the other hand, the M–O distances remain the same for **1–3** and significantly increase in the case of Ni^{II} complex **4** due to the Jahn–Teller effect,[71] which is typical of structurally similar seven-coordinate pentagonal bipyramidal Ni^{II} complexes $[NiL1Cl_2]$,[72] $[NiL2](ClO_4)_2$,[12] [NiL3],[38] $[NiL6](ClO_4)_2$ [35] for which the Ni–O distances often exceed 2.5 Å. Thus, the pentagonal bipyramidal geometry of the Ni^{II} centre in **4** is the most distorted one (Ni–O is 2.413(2) and 2.416(2) Å) and this distortion for the second crystallographically independent molecules present in the asymmetric

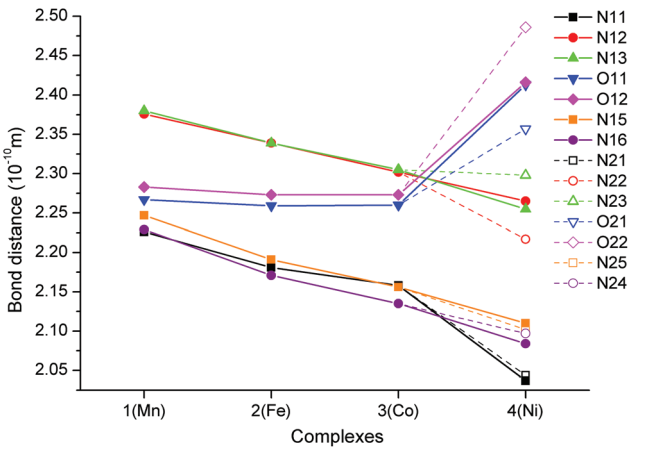

Fig. 3 Comparison of the metal–donor atom distances in complexes **1–4** depending on the type of the central metal atom. The empty symbols and dashed lines correspond to the values for the second crystallographically independent molecule present in the asymmetric unit in **4**. The lines serve as guides.

Table 1 Selected interatomic distances [Å] and angles [°] of compounds **1–4**

Distances	1	2	3	4
M–N11/21	2.230(3)/2.226(3)	2.184(3)/2.181(3)	2.166(2)/2.158(3)	2.044(2)/2.037(2)
M–N12/22	2.381(3)/2.376(3)	2.334(3)/2.339(3)	2.300(2)/2.302(2)	2.217(2)/2.265(2)
M–N13/23	2.378(3)/2.380(3)	2.340(3)/2.339(3)	2.304(2)/2.305(2)	2.298(2)/2.255(2)
M–O11/21	2.278(2)/2.267(2)	2.260(2)/2.259(2)	2.264(2)/2.260(2)	2.357(2)/2.413(2)
M–O12/22	2.281(2)/2.283(2)	2.280(2)/2.273(2)	2.281(2)/2.273(2)	2.486(2)/2.416(2)
M–N16/24	2.241(3)/2.247(3)	2.178(3)/2.191(3)	2.147(2)/2.156(2)	2.097(2)/2.110(2)
M–N15/25	2.251(3)/2.229(3)	2.186(3)/2.171(3)	2.145(2)/2.135(2)	2.102(2)/2.084(2)
Angles[a]				
N11–M–N12	71.54(9)	71.95(9)	72.09(9)	76.10(8)
N12–M–O11	74.89(8)	74.89(9)	74.54(8)	75.04(7)
O11–M–O12	72.00(8)	70.69(8)	70.74(7)	66.44(6)
N13–M–O12	73.63(8)	73.47(9)	73.20(8)	70.45(7)
N11–M–N13	70.99(9)	71.54(9)	71.75(9)	74.08(8)
N11–M–N15	92.62(9)	93.60(10)	93.11(9)	95.63(8)
N12–M–N15	104.57(9)	104.88(9)	103.06(9)	103.57(8)
N13–M–N15	76.39(9)	77.27(9)	78.89(9)	79.54(8)
O11–M–N15	84.43(9)	84.78(9)	84.66(9)	82.46(8)
O12–M–N15	87.54(9)	86.51(9)	87.65(8)	85.22(7)
N11–M–N16	97.83(9)	97.76(9)	97.07(9)	99.13(8)
N12–M–N16	75.60(9)	76.61(9)	78.11(9)	79.99(8)
N13–M–N16	110.42(9)	108.59(9)	106.42(9)	104.64(8)
O11–M–N16	84.98(9)	84.53(9)	85.71(9)	84.71(8)
O12–M–N16	86.19(9)	85.69(9)	85.42(8)	82.98(7)
N15–M–N16	168.95(10)	168.39(10)	169.58(9)	165.24(8)

[a] Values for one of the two crystallographically independent molecules present in the asymmetric unit of each complex are given.

unit is even more pronounced (Ni–O is 2.357(2) and 2.486(2) Å, see Table 1 and Fig. 3 – empty symbols). This observation was confirmed by an analysis of the geometry of coordination polyhedra of all complexes **1–4** based on a comparison of continuous shape measures obtained by program Shape 2.1 (deviation between the real and ideal geometry of the polyhedron, Table S2†),[73,74] because the lowest deviation values were obtained for the pentagonal bipyramidal arrangement.

The final crystal packing of all studied complexes **1–4** is influenced by π–π stacking interactions between the benzimidazole units in the pendant arms (centroid⋯centroid distance $C_g \cdots C_g$ = 3.664/3.665/4.016/4.563 Å (**1**), 3.672/3.673/4.035/4.549 Å (**2**), 3.679/3.680/4.060/4.605 Å (**3**), and 3.668/3.678/4.057/4.620 Å (**4**)), which are responsible for the formation of supramolecular linear 1D chains along the *c*-axis (Fig. 4). Each supramolecular 1D chain contains only one enantiomeric form of the complex cation and these 1D chains regularly alternate in the final crystal packing as shown in Fig. 4. Furthermore, these 1D chains are connected to each other by a large number of hydrogen bonds (N–H⋯O–Cl, C–$H_{aromatic}$⋯O–Cl, C–$H_{aromatic}$⋯O–N) among the perchlorate counter-ions, complex cations and nitromethane solvent molecules.

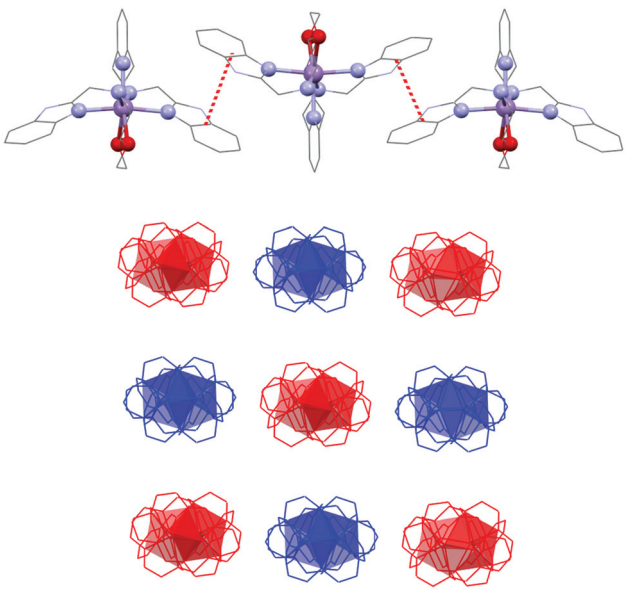

Fig. 4 (top) Part of the crystal structure of **1** showing a supramolecular 1D chain of individual $[MnL]^{2+}$ complex cations connected together by π–π stacking interactions (red dashed lines). (bottom) View along the *c* axis on the arrangement of supramolecular 1D chains of the $[ML]^{2+}$ complex cations in **1** with an indication of their enantiomeric forms (red for $[Mn(S,S)\text{-}L]^{2+}$, blue for $[Mn(R,R)\text{-}L]^{2+}$).

Comparison of the obtained molecular structures with those of previously studied complexes containing L2 and L3

The molecular structure of metal complexes is crucial for understanding their magnetic anisotropy (see the next section Magnetic analysis) and therefore it is important to compare the obtained molecular structures of the Fe^{II}, Co^{II} and Ni^{II} complexes containing **L** with those of previously studied complexes containing structurally similar ligands **L2** and **L3** (Fig. 5) in order to reveal any trends which could explain the observed magnetic properties.

The N_{py}–M distance does not change much going from **L** to **L3** for all three metals, but its value decreases from Fe^{II} to Ni^{II} according to the decreasing ionic radius. The N(1,2-aliphatic)–

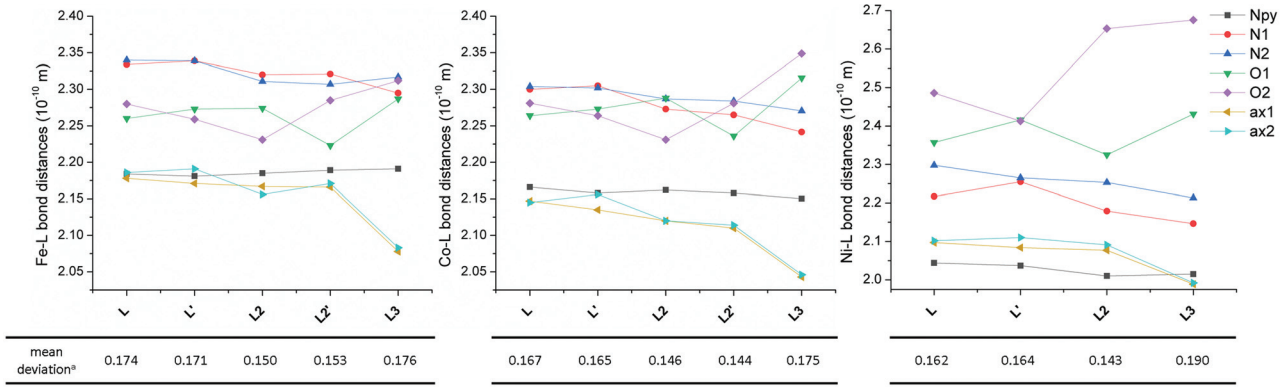

Fig. 5 Comparison of the bond distances for Fe^{II} (left), Co^{II} (middle) and Ni^{II} (right) complexes of studied ligand **L** as well as the complexes of previously studied structurally similar ligands **L2** and **L3**. [a]Mean deviation of all equatorial donor atoms (N_3O_2) from the least-squares plane defined by the ligand donor atoms in the equatorial plane and the central metal atom (MN_3O_2). The lines serve as guides. Data for both crystallographically independent molecules (indicated by apostrophe) found in the asymmetric unit are given.

M distances almost always decrease for **L** → **L3** (only the N2–M distance slightly increases in the case of the Fe^{II} complex when going from **L2** to **L3**). On the other hand, the effect on the O–M distances is opposite. When going from **L** to **L2**, one distance decreases while the other increases for all metals (but the mean values for both crystallographically independent molecules slightly decrease), but both values increase when going from **L2** to **L3**. The most significant increase is observed for the Ni^{II} complex due to the operating Jahn–Teller effect. The distances between the metal and axial donor atoms decrease when going from **L** to **L3** for all three metals. This indicates, in comparison with **L**, stronger axial binding in the case of pyridine analogue **L2** (both **L** and **L2** are neutral) and a significant electrostatic contribution in the case of negatively charged carboxylate analogue **L3**.

Thus when going from **L** to **L3** in all Fe^{II}, Co^{II} and Ni^{II} complexes, the metal in the equatorial plane is shifted towards the N-donor containing part and moving away from the O-donor part of the macrocycle, and the axial donor atoms are getting closer to the metal atom. One has to also pursue the variation of the distances in the equatorial plane, because the observed axial compression of the pentagonal bipyramid (**L** → **L3**) resulted either in a more symmetric equatorial plane in the case of the Fe^{II} complex of **L3** (the N–M and O–M distances are close to each other) or in a more asymmetric equatorial plane in the case of Co^{II} and especially the Ni^{II} complex of **L3** (the N–M and O–M distances are very different). From Fig. 5, it is also evident that the M–O distances in comparison with M–N (aliphatic) are shorter in the case of Fe^{II} complexes, are comparable in the case of Co^{II} complexes and longer in the case of Ni^{II} complexes, which is in accordance with the oxophilic character of Fe^{II} and N-donors preference for Ni^{II}.

Moreover, an additional interesting parameter is the planarity of the equatorial plane, which can be described by the mean deviation of equatorial donor atoms (N_3O_2) from the least-squares plane defined by the central metal atom and all equatorial donor atoms (MN_3O_2). The complexes with the most planar equatorial plane form pyridine ligand **L2** followed by benzimidazole ligand **L** and carboxylate ligand **L3** (Fig. 5). In the case of complexes with **L** and **L2**, the planarity increases from Fe^{II} to Ni^{II} (the mean deviation decreases), while in the case of complexes with **L3**, the lowest planarity (the highest mean deviation) is observed for the Ni^{II} complex. But in general, it can be concluded that the equatorial planarity of all complexes (similar structural types) is comparable.

Magnetic analysis

Static magnetic measurements. The temperature- and field-dependent experimental magnetic data for **1–4** are depicted in Fig. 6. The room temperature values of the effective mag-

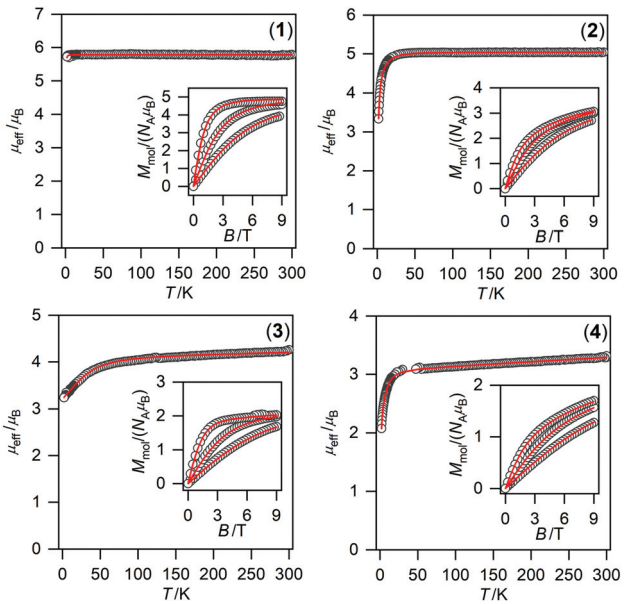

Fig. 6 Magnetic data for compounds **1–4**. Temperature dependence of the effective magnetic moment and the isothermal magnetizations measured at T = 2, 5, and 10 K. The empty circles represent the experimental data points and the full lines represent the best fits calculated by using eqn (1) with parameters listed in Table 2.

netic moment (μ_{eff}/μ_B) are close to the theoretical values for the high-spin divalent metal complexes (μ_{eff}/μ_B = 5.92 for S = 2.5 (Mn^{II}), μ_{eff}/μ_B = 4.90 for S = 2 (Fe^{II}), μ_{eff}/μ_B = 3.87 for S = 3/2 (Co^{II}) and μ_{eff}/μ_B = 2.83 for S = 1 (Ni^{II})). Upon lowering the temperature, there is a significant drop in the effective magnetic moment observed for compounds **2–4** indicating significant magnetic anisotropy, and hence zero-field splitting (ZFS). This is also supported by the lower values of the isothermal magnetization at the highest applied magnetic field in comparison with the theoretically expected values derived by the Brillouin function as $M_{mol}/N_A\mu_B = g{\cdot}S$, where S = 2 for **2**, S = 3/2 for **3** and S = 1 for **4**. In contrast, the situation for **1** is much different: the μ_{eff} value is almost constant in the whole temperature range and also the isothermal magnetization is close to the Brillouin function, which indicate minute ZFS in **1** as expected for the $3d^5$ electronic configuration.

Thus, the experimental magnetic data were treated with the spin Hamiltonian comprising ZFS terms describing the magnetic anisotropy and Zeeman term postulated as

$$\hat{H} = D(\hat{S}_z{}^2 - \hat{S}^2/3) + E(\hat{S}_x{}^2 - \hat{S}_y{}^2) + \mu_B B g \hat{S}_a \quad (1)$$

where D and E are the single-ion axial, and rhombic ZFS parameters, respectively, and the last component represents the Zeeman term defined in a direction of the magnetic field as $B_a = B(\sin(\theta)\cos(\varphi), \sin(\theta)\sin(\varphi), \cos(\theta))$ with the help of the polar coordinates.[75] Then, the average molar magnetization corresponding to the powder samples was calculated.

To obtain reliable parameters, both temperature and field-dependent magnetic experimental data were fitted concurrently. The best-fitted parameters are listed in Table 2.[76] The large and negative D-value was found for Ni^{II} compound **4** (−17.2 cm^{-1}) whereas the large and positive D-values were found for Co^{II} and Fe^{II} compounds **3** (40.3 cm^{-1}) and **2** (7.9 cm^{-1}), respectively. This is in accordance with the different low temperature values of μ_{eff}/μ_B observed for **2–4** (Fig. 6).

When the obtained D-values are compared with those of previously studied complexes with **L2** and **L3** (Table 2),[12,38] they are very similar for Mn^{II} and Fe^{II} complexes **1** and **2**, but they are much higher for Co^{II} and Ni^{II} complexes **3** and **4** revealing their larger magnetic anisotropy. The sign of the D-value for **2** is positive and thus different from previously studied Fe^{II} complexes with **L2** and **L3** (Table 2), but it is in accordance with the CASSCF/NEVPT2 calculations for **2** (Table 2) and also with the previously performed calculations (see Fig. 10 in ref. 38). These calculations showed that the strong axial ligand field in the seven-coordinate Fe^{II} complex can provide small positive D-values while when this ligand field is reduced, D becomes larger and negative. Moreover, HF-EPR measurements (Fig. S5†) confirmed the positive sign of D. The data for 180 GHz, 321 GHz and 415 GHz at 4 K were successfully simulated for the spin S = 2 with D = +8.2 cm^{-1} and E/D = 0.29 and the g values from Table 2. The EPR signal vanishes at 15 K, in agreement with the simulated data, which indicates a significant decrease in the absorption intensity with increasing temperature. Both complexes **3** and

Table 2 Comparison of *ab initio* calculated and fitted spin Hamiltonian parameters for complexes **1–4**[a] and for the complexes with **L2** and **L3**

Compound	**1**	**2**	**3**	**4**
Central metal atom	Mn(II)	Fe(II)	Co(II)	Ni(II)
Electron configuration	$3d^5$	$3d^6$	$3d^7$	$3d^8$
Spin state S	5/2	2	3/2	1
	ZFS and g values based on CASSCF/NEVPT2 calculations			
D (cm^{-1})	−0.071/−0.076	7.41/7.55	34.4/34.0	−23.8/−25.6
E/D	0.101/0.087	0.200/0.183	0.082/0.085	0.067/0.043
g_x	2.000/2.000	2.079/2.081	2.320/2.312	2.251/2.245
g_y	2.000/2.000	2.172/2.175	2.383/2.378	2.233/2.234
g_z	2.000/2.000	2.017/2.016	2.042/2.041	2.404/2.414
	ZFS values based on CASSCF/DCD-CAS(2) calculations			
D (cm^{-1})	−0.114/−0.122	7.67/7.80	38.4/37.9	−23.6/−25.5
E/D	0.069/0.070	0.145/0.122	0.067/0.074	0.062/0.040
	Magnetic analysis of the experimental data[b]			
D (cm^{-1})	−0.30(3)	7.90(6)	40.3(1.5)	−17.2(2)
E/D	0.0	0.220(4)	0.10(3)	0.076(1)
g	1.9538(9)	2.057(1)	g_{xy} = 2.156(6) g_z = 2.00	2.165(3)
χ_{TIP} (10^{-9} m^3 mol^{-1})	0.0	0.0	5.3(5)	7.5(2)
	Data for complexes with **L2**[12]			
D (cm^{-1})	0	−7.4	34.0	−12.8
E/D		0.0	0.0	0.136
	Data for complexes with **L3**[38]			
D (cm^{-1})	—	−9.6	29.1	−8.5
E/D		0.006	0	0.19

[a] The theoretical calculations were done for both crystallographically independent molecules present in the asymmetric unit. [b] The detailed procedure for the calculation of standard deviations is described in ref. 76.

Table 3 List of mononuclear seven-coordinate Co^{II} SMMs together with the obtained ZFS parameters and parameters describing the relaxation of magnetization

Complex	ZFS		Orbach		Direct	Raman		Ref.
	D/cm^{-1}	E/D	$\tau_0/10^{-9}$ s	U_{eff}/cm^{-1} (K)	A/K^{-1} s^{-1}	C/K^{-n} s^{-1}	n	
[Co(H$_2$**L4-Ph**)(H$_2$O)(NO$_3$)]NO$_3$	32.4	0	0.6	56.3 (81.2)				17,18
[Co(15-pydienN$_5$)(H$_2$O)$_2$]Cl$_2$	24.6	−0.014	1200	20.7 (29.8)				18
[Co(**L4-Ph**)(im)$_2$][a]	24.8	0.0016	0.087	62.3 (89.6)				18
[Co(**tbp**)$_3$(NO$_3$)$_2$][a]	35.8	0.006	768	17.7 (25.5)				78
[Co(**isq**)$_3$(NO$_3$)$_2$][a]	35.7	0.0006	701	11.0 (15.8)				78
[Co(**L5**)(H$_2$O)$_2$](BF$_4$)$_2$	25.6	−0.039	1100	42.2 (29.3)				19
[Co(**L5**)(CN)$_2$]·2H$_2$O	17.4	−0.034	3200	48.9 (34.0)				19
[Co(**L5**)(NCS)$_2$]	26.3	−0.004	1000	49.2 (34.2)				19
[Co(**L5**)(SPh)$_2$]	34.5	−0.052	2100	54.7 (38.0)				19
[Co(**L1**)Cl$_2$]·2CH$_3$OH	38(3)	0	—[b]	5.5–7.8 (7.9–11.2)[b]		0.99–1.62[b,c]	1.76–2.59[b]	21
[Co(**L1**)Br$_2$]	41(1)	0	1120	4.2 (6.1)		613	2.79	21
[Co(**L1**)I$_2$]	35(1)	0	1120	4.5 (6.5)		500	2.82	21
[Co(**L2**)](ClO$_4$)$_2$	34	0	990	16.9 (24.3)		47.3	2.84	12
[Co(**L3**)]·H$_2$O	29.0	0	—	—	96.9	0.535	5.49	38
[Co(15-pydienN$_3$O$_2$)(CH$_3$CN)$_2$](BPh$_4$)$_2$	36.9	0.005	0.034(2)	62 (89)		131(9)	2.1(1)	79
[Co(**L4-PhOH**)(CH$_3$OH)$_2$]	43.1	0.077	7400	23.3 (33.5)			4.7	22
[Co(H$_2$**L4-PhOH**)(NCS)(CH$_3$OH)]ClO$_4$·CH$_3$OH	41.5	0.036	5600	19.7 (28.4)			4.2	22
[Co(H$_2$**L4-PhOH**)(NCS)$_2$]·2CH$_3$OH	38.8	0.54	4800	16.4 (23.6)			3.7	22
[Co(H$_2$**L4-NH$_2$**)(NCS)$_2$]·0.5C$_2$H$_5$OH	35.6	0.17	—	—	1.03×10^{-3} [d]	0.00106	9[e]	33
[Co(H$_2$**L4-NH$_2$**)(NCSe)$_2$]·0.5C$_2$H$_5$OH	38.2	0	—	—	4.10×10^{-4} [d]	0.02	7.4	33
[Co(H$_2$**L4-NH$_2$**){N(CN)$_2$}$_2$]·2H$_2$O	35.3	0.101	—	—	1.29×10^{-4} [d]	0.017	7.3	33
[Co(H$_2$**L4-NH$_2$**)(H$_2$O){C(CN)$_3$}]NO$_3$·1.16H$_2$O	33.6	0.149	—	—	7.7×10^{-5} [d]	0.4	5.6	33
{[Co(H$_2$**L4-NH$_2$**)(H$_2$O)(N$_3$)]-[Co(H$_2$**L4-NH$_2$**)(N$_3$)$_2$]}N$_3$·4H$_2$O	40.4	0	—	—	2.9×10^{-4} [d]	0.26	5.8	33
[Co(**L**)](ClO$_4$)$_2$·1.5CH$_3$NO$_2$	40.3	0.1	6040	6.0 (8.7)		507	2.58	This work

[a] im = imidazole, tbp = 4-*tert*-butylpyridne, isq = isoquinoline. [b] Calculated by a simplified model described in the corresponding literature. [c] Values correspond to $2\pi f/C$ (where f is the AC frequency). [d] In the unit Oe^{-2} K^{-1} s^{-1}. [e] Fixed during the fitting procedure.

4 show the highest magnetic anisotropies among those reported for the pentagonal bipyramidal Co^{II} (Table 3) or Ni^{II} complexes (Table 2). If the calculations previously reported by Sutter and Mallah are considered,[17] the stronger axial ligand field should provide larger magnetic anisotropy in the case of Ni^{II} complexes, while an opposite effect on the magnetic anisotropy is expected for the Co^{II} complexes. A similar trend as for the Ni^{II} complexes was recently observed for the Fe^{II} complexes,[11] but the description/explanation was more complex concerning the contribution(s) to the D value from different excited states and also differential π-interactions of the Fe^{II}–axial ligands between the x and y directions. Thus, according to the large magnetic anisotropy of Co^{II} complex **3**, the axial field should be weaker, but on the other hand according to the large magnetic anisotropy of Ni^{II} complex **4** and the positive sign of D for Fe^{II} complex **3**, the axial field should be stronger. So, not only the axial, but also the equatorial effect (a more symmetric field provides larger anisotropy) should be taken into account, which makes the elucidation of any trend for the complexes of *N*-pendant armed macrocycles not as straightforward as expected. We tried to establish such a magneto-structural correlation as shown in Fig. 7, where the average equatorial and the axial metal to the donor atom distances together with the values of the D-parameter are shown for each metal ion as a function of coordinated ligands (**L**, **L2** and **L3**). The D value is becoming more positive for both Fe^{II} and Co^{II} complexes, while D is becoming more negative for the Ni^{II} complexes considering the change of ligands, **L3** → **L** (Fig. 7).

If we consider that the increasing average distance of axial donor atoms (**L3** → **L**) can be interpreted in terms of a weaker axial ligand field (although benzimidazole is a stronger σ-donor than pyridine, it is also a weaker π-acceptor),[40] the increasing magnetic anisotropy of the Co^{II} complexes is in agreement with the theoretically predicted trend. This is in contrast to the behavior of the Ni^{II} complexes, where the magnetic anisotropy increased twice (**L3** → **L**), which can be rather explained by the more symmetric equatorial ligand field (Fig. 5, right) and this can be quantified by deviations from the PBPY-7 ideal symmetry obtained by the program SHAPE (1.112 and 1.201 for **L**, Table S2,† 1.237 for **L2**,[12] and 2.988 for **L3**).[38] As the change in the equatorial ligand field has a more dramatic impact on the value of D than on the variation of the axial ligand field in the Ni^{II} complexes (see Fig. 12 later in the section, Theoretical calculations), the increase of negative D for the Ni^{II} complexes (**L3** → **L**) is more likely governed by the decreasing deviation from the ideal D_{5h} symmetry. The absolute values of D and $|D|$ for the Fe^{II} complexes are almost the same, which is in agreement with our theoretical simulations (*vide infra*) showing a small impact of the ligand field change on the size of the magnetic anisotropy. Moreover, the variation of ZFS parameters for the Fe^{II} complexes must be considered with great care, because usually the low lying excited states reduce the validation of the spin Hamiltonian approach.

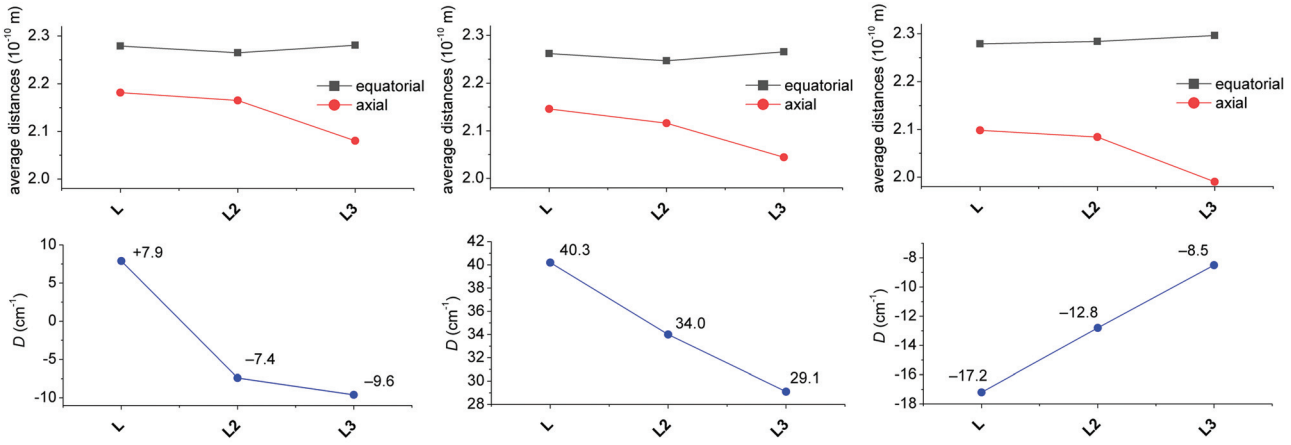

Fig. 7 Magneto-structural correlation for the Fe^{II} (left), Co^{II} (middle) and Ni^{II} (right) complexes of studied ligand **L** and previously studied structurally similar ligands **L2** and **L3**. Variation of the average bond distance in the equatorial plane and in axial positions (top) and variation of the axial zero-field-splitting parameter *D* (bottom). The lines serve as guides. If two crystallographically independent molecules were found in the asymmetric unit, the average values are given.

In conclusion, both axial and equatorial ligand fields have to be considered when analyzing the magnetic anisotropy, because the change in each field has a differently strong and sometimes opposite impact on the resulting anisotropy. Moreover these effects have different extents for different central metal ions and thus, general analysis for more metals appears to be intricate.

Dynamic magnetic measurements

The alternating current (AC) susceptibly measurement was performed for **2–4**, however, the non-zero out-of-phase signal was found only for Co^{II} compound **3** upon applying a weak static magnetic field (Fig. S6†). Therefore, temperature and frequency dependent AC susceptibility data were acquired at B_{DC} = 0.1 T (Fig. 8) and clearly defined maxima of the out-of-phase signal of AC susceptibility dependent on the applied frequency were found for compound **3**, which is the characteristic behavior of SMMs. Next, the one-component Debye's model was applied based on the equation

$$\chi(\omega) = \frac{\chi_T - \chi_S}{1 + (i\omega\tau)^{1-\alpha}} + \chi_S \qquad (2)$$

which resulted in isothermal (χ_T) and adiabatic (χ_S) susceptibilities, relaxation times (τ) and distribution parameters (α) (Table S3†). Afterwards, the Argand (Cole–Cole) plot was constructed as shown in Fig. 8. The application of the Arrhenius law to the temperature dependence of the relaxation times revealed $\tau_0 = 6.04 \times 10^{-6}$ s and $U_{eff} = 6.0$ cm^{-1} (8.7 K). Such a physically unreasonable value of U_{eff} can be ascribed to the fact that the *D*-parameter is positive and *E*/*D* is very small, hence, the easy-plane type of magnetic anisotropy is operational, which means that there is no energy barrier *U* defined by $|D|(S^2 - \frac{1}{4})$. The origin of the slow relaxation of magnetization in Kramers ions (such as Co^{II}) with dominant easy-plane magnetic anisotropy was investigated in detail by E. Ruiz, F. Luis *et al.*,[77] and such spin–lattice relaxation was rather

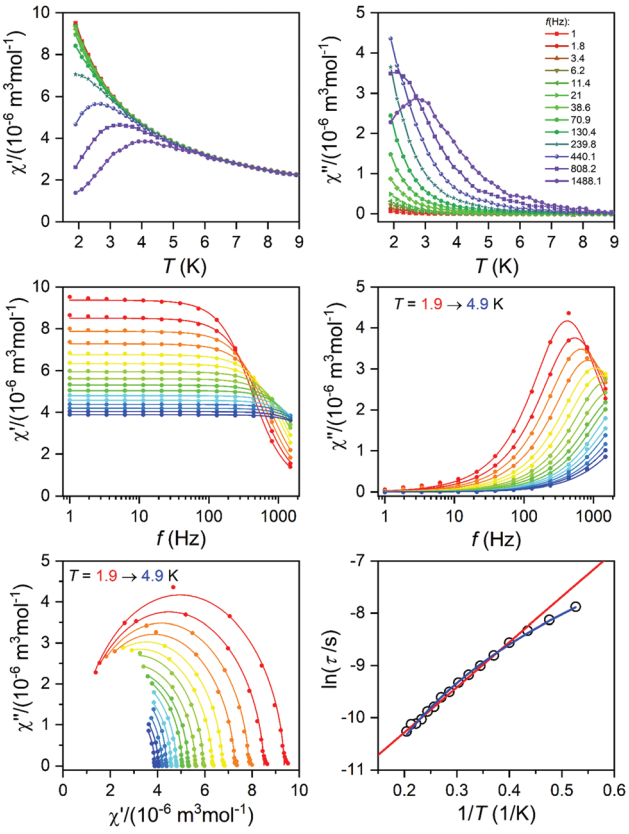

Fig. 8 AC susceptibility data of **3**. Top: in-phase χ' and out-of-phase χ'' molar susceptibilities at the applied external magnetic field B_{DC} = 0.1 T (the full lines are only guides for the eye). Middle: frequency dependence of in-phase χ' and out-of-phase χ'' molar susceptibilities. The full lines represent the fitted data using eqn (2). Bottom: the Argand (Cole–Cole) plot with a full line fitted with eqn (2) and the fit of the resulting relaxation times τ with the Arrhenius law (red line) and Raman relaxation process (blue line).

described by one-phonon direct processes and two-phonon Raman processes. Therefore, the temperature dependence of the relaxation times was successfully fitted considering the Raman relaxation mechanism described by the following equation

$$\frac{1}{\tau} = CT^n \quad (3)$$

with C = 507 K^{-n} $s^{-1}$and n = 2.58 (Fig. 8). Similar values of n were also reported for other seven-coordinate Co^{II} complexes (Table 3).[12,21] Here we also note that the inclusion of the direct term in eqn (3) did not lead to a better fit.

The obtained values of τ_0 and U_{eff} for the Orbach relaxation process or C and n for the Raman relaxation process are compared with those of previously studied pentagonal bipyramidal Co^{II} SMMs in Table 3. The U_{eff} values are comparable with those of the Co^{II} complexes with structurally similar ligands **L1**, **L2**, and **L3**, but are smaller in comparison with those of other ligands having a more rigid macrocyclic part (**15-pydienN_3O_2**, **L4-Ph**, **L5**). This "equatorial rigidity" effect appears to have a more significant influence on the relaxation times than on the magnetic anisotropy represented by the D-value. Thus, there is no clear relationship between the magnetic anisotropy (D) and the values of relaxation times, which can be attributed to the fact that the Orbach relaxation mechanism is not active for such easy-plane systems and the direct and Raman relaxation processes should stand at the centre of our focus. Therefore, in order to increase the relaxation time, the C and n parameters of the Raman relaxation process should be decreased. However, the lack of these parameters from the literature means that further investigation of Co^{II} complexes has to be done to better understand the relationship between the molecular structure and relaxation properties.

Electrochemistry

In order to investigate the electrochemical properties of prepared complexes **1–4**, the measurement of cyclic voltammetry was performed in acetonitrile solution. The obtained cyclic voltammograms are depicted in Fig. 9 and the redox potentials are listed in Table 4. All $E_{1/2}$ potentials for the $Mn^{3+/2+}$, $Fe^{3+/2+}$ and $Co^{3+/2+}$ couples are very high (1.596, 1.043 and 1.853 V, respectively), which indicates that the lower oxidation states ($Mn^{2+}/Fe^{2+}/Co^{2+}$) are stabilized due to the π-acceptor ability of axially coordinated two benzimidazolyl pendant arms. Moreover, the $Ni^{3+/2+}$ redox couple is not even visible in the range of available potentials during the measurement. Thus, the oxidation state $^{+III}$ of the Ni^{II} complexes is not accessible, which is in accordance with the π-acceptor properties of benzimidazole functional groups. On the other hand, lower oxidation states $Mn^{+}/Fe^{+}/Co^{+}/Ni^{+}$ are accessible in quasi-reversible/quasi-reversible/reversible/quasi-reversible processes at relatively high negative potentials (see Table 4). Furthermore, irreversible reduction peaks at *ca.* −1.25 and −1.40 V were detected and they correspond to the reduction of the CH_3NO_2 co-crystallized solvent molecule as was confirmed by the measurement of MeCN solution with an extra addition of CH_3NO_2 (Fig. S7†).

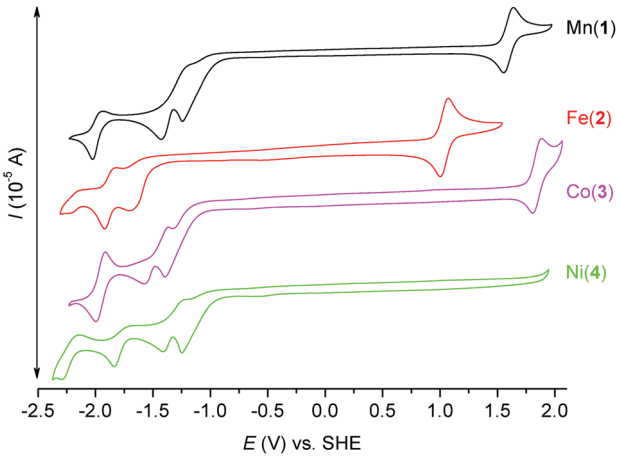

Fig. 9 Cyclic voltammograms of complexes **1** (black), **2** (red), **3** (purple), and **4** (green) (~2 mM) recorded under an argon atmosphere in 0.1 M TBAP in acetonitrile with a glassy carbon working electrode. Complex **2** was the only one used for the measurement in its form prior to recrystallization from CH_3NO_2.

Table 4 Results of cyclic voltammetry experiments

Compound	Redox process	$E_{1/2}$ [V] *vs.* Fc/Fc^+	$E_{1/2}$ [V] *vs.* SHE	ΔE [mV]
1	Mn^{3+}/Mn^{2+}	0.972	1.596	84
	Mn^{2+}/Mn^{+}	−2.604	−1.980	91
2	Fe^{3+}/Fe^{2+}	0.419	1.043	70
	Fe^{2+}/Fe^{+}	−2.496	−1.872	93
3	Co^{3+}/Co^{2+}	1.229	1.853	76
	Co^{2+}/Co^{+}	−2.584	−1.960	80
4	Ni^{2+}/Ni^{+}	−2.375	−1.751	140

The cyclic voltammogram of the ligand **L** was measured as well and it shows one irreversible oxidation peak at E_{ox} = 1.450 V (Fig. S8†), which may be assigned to the oxidation of both benzimidazolyl pendant arms, and one irreversible reduction peak at E_{red} = −2.063 V.

When the obtained results are compared with those of the complexes containing structurally similar pyridine analogue **L2**, several aspects can be found. The $E_{1/2}$ potentials for the $Mn^{3+/2+}$ and $Fe^{3+/2+}$ couples are slightly lower than those found for the complexes with **L2** ($E_{1/2(Mn)}$ = 1.624 V, $E_{1/2(Fe)}$ = 1.132 V *vs.* SHE, see Fig. S9 and S10†), but the $E_{1/2}$ potential for the $Co^{3+/2+}$ couple is slightly higher than that for the complex with **L2** ($E_{1/2(Co)}$ = 1.744 V *vs.* SHE, see Fig. S11†).[80] Therefore the oxidation states Mn^{2+} and Fe^{2+} are more stabilized in the complexes with **L2**, while the oxidation state Co^{2+} is more stabilized in the complex with **L**. On the other hand, lower oxidation states $Mn^{+}/Fe^{+}/Co^{+}$ are easily accessible in the complexes with **L2** because complexes **2–4** with **L** have more negative reduction potentials (see Fig. S9–S11†). This is in accordance with the weaker π-acceptor ability of the benzimidazole moiety in comparison with the pyridine one. In conclusion the electrochemical behavior of the complexes with **L** and **L2** is rather similar, but in the case of the complexes with **L** the lower oxi-

dation states are less accessible and thus, the oxidation state +II is more stabilized.

Theoretical calculations

The electronic structure of the reported complexes was also studied by theoretical methods using computational package ORCA 4.1. First, the post-Hartree–Fock multireference calculations based on the state-averaged complete active space self-consistent field method (SA-CASSCF) were employed together with the def2-TZVP basis set to reveal the impact of the spin–orbit coupling and ligand field on the spin Hamiltonian parameters, especially on the zero-field splitting parameters D and E. The active space was defined by n-electrons in five d-orbitals, CAS(n,5), and we have used two methods to cover the dynamic electron correlation effect, namely, the well-known N-electron valence state perturbation theory (NEVPT) and also the recently introduced dynamic correlation dressed CAS with the second-order treatment (DCD-CAS(2)). The *ab initio* ligand field theory (AILFT)[81,82] was used to calculate the energy of the d-orbitals as depicted in Fig. 10. The ideal D_{5h} ligand field symmetry leads to splitting of the d-orbitals into three sets, e_1'' (d_{xz}, d_{yz}), e_2' (d_{xy}, $d_{x^2-y^2}$) and a_1' (d_{z^2}), and such a pattern is visible in the case of **1**, but even in this complex, the degeneracy of the d-orbitals is removed due to the non-homogenous ligand field. Evidently, the pattern of the splitting of the d-orbitals is continuously changing from **1** to **4** and is interconnected with the weakening of M–O donor–acceptor bonds.

Subsequently, the ligand-field terms are shown in Fig. 10 and it is evident that except for **1**, there are close lying terms with the same or lower multiplicities which do contribute to the zero-field splitting of the ground spin state multiplet (Fig. 10, right). The calculated ZFS and g-tensor parameters are summarized in Table 2, where calculations for both metal complexes within asymmetric units were done. The reported values are in very good agreement with the fitted ones, especially for compounds **2** and **3**, *e.g.* D = 38.4/37.9 cm^{-1} for **3**

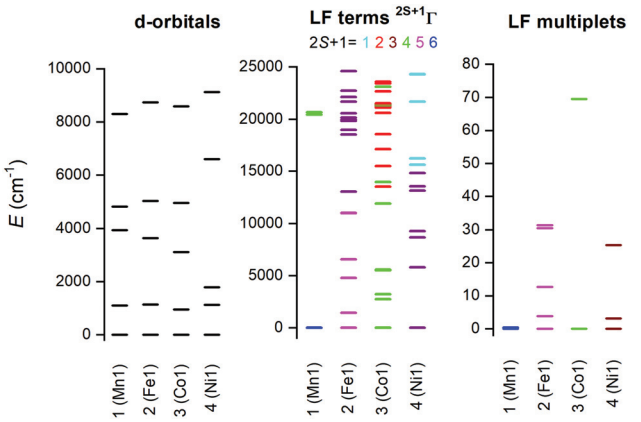

Fig. 10 Graphical output of the CASSCF/NEVPT2 calculations for the mononuclear molecular fragments $[ML]^{2+}$ of **1**–**4**. Plot of the d-orbitals splitting calculated by the *ab initio* ligand field theory (AILFT) (left), low-lying ligand-field terms with various multiplicities (middle), and ligand-field multiplets (right).

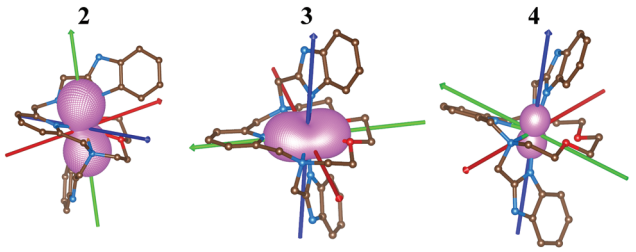

Fig. 11 The molecular structures of **2**–**4** derived from the experimental X-ray geometries used for the CASSCF/NEVPT2 calculations overlaid with the three-dimensional plot of the calculated molar magnetization at T = 2 K and B = 1 T and also showing principal axes of D-tensors (x/y/z-axes colored as red/green/blue arrows). The hydrogen atoms are not shown.

derived by DCD-CAS(2) and the fitted value of D is 40.2 cm^{-1}. The main axes of the calculated D-tensors for the complexes with large magnetic anisotropy, **2**–**4**, are shown in Fig. 11 together with a three-dimensional plot of the calculated molar magnetization. Evidently, the easy-plane type of the magnetic anisotropy is present in the Co^{II} complex and coincides with the equatorial pentagonal plane, while the easy-axis type is found in both Fe^{II} and Ni^{II} complexes. In the case of Ni^{II}, this behavior is natural due to the negative value of the D-parameter, however, in the case of Fe^{II}, the D-parameter is positive but due to large rhombicity, the easy-axis type of the magnetic anisotropy is operational.

With the aim to get more insight into the role of the equatorial and the axial ligand field strength in the zero-field splitting of such pentagonal bipyramidal complexes of late transition metal complexes, we performed the CASSCF/DCD-CAS(2) calculations for model complexes $[M(NH_3)_2(NCH)_3(H_2O)_2]^{2+}$ (M = Fe^{II}, Co^{II} and Ni^{II}) – Fig. 12. Both the in-plane and the axial metal-donor interatomic distances were varied in the range from 1.9 to 2.5 Å, which enabled the creation of the contour plots of the axial and rhombic ZFS parameters – Fig. 13.

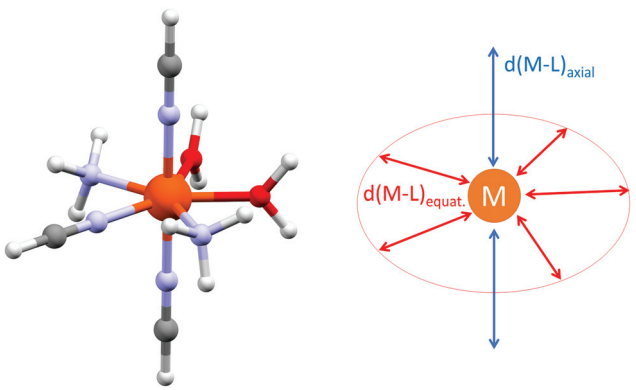

Fig. 12 The general molecular structure of the model complexes $[M(NH_3)_2(NCH)_3(H_2O)_2]^{2+}$ (M = Fe^{II}, Co^{II} and Ni^{II}) together with the depiction of the varied structural parameters used for the CASSCF/DCD-CAS(2) calculations.

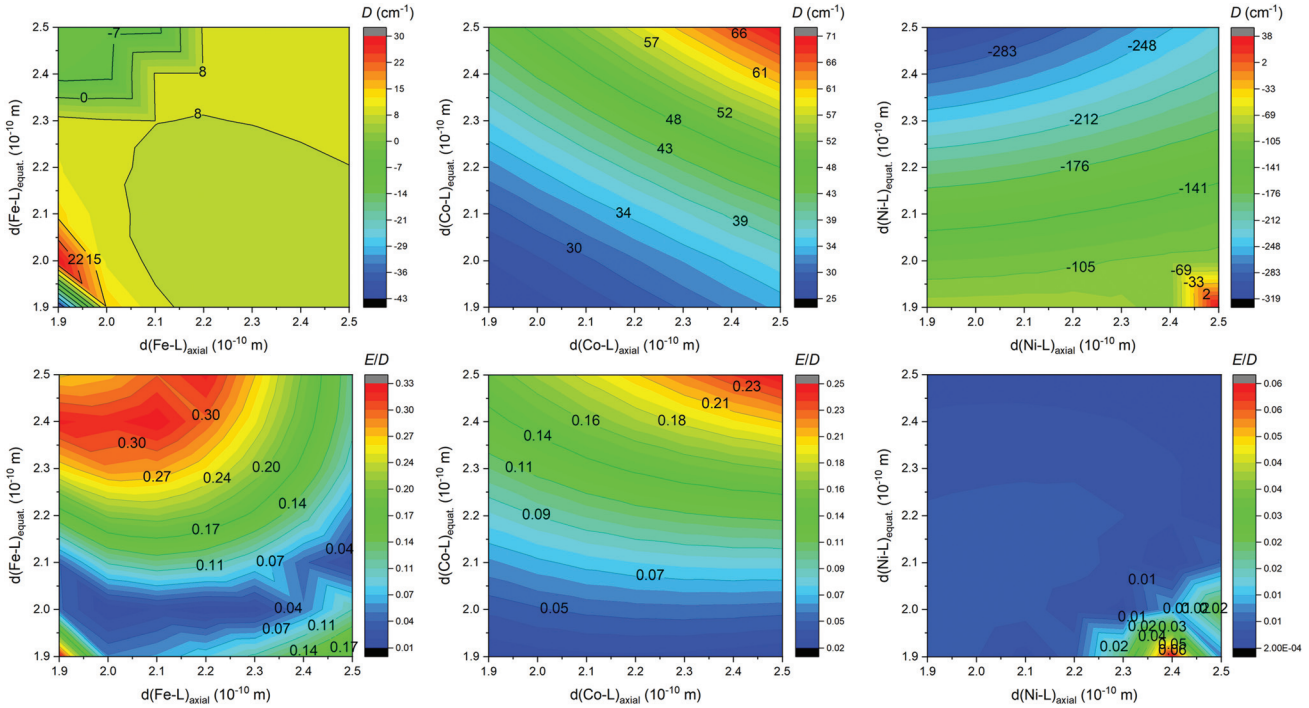

Fig. 13 The contour plot showing the impact of variation of the ligand field of the axial and the equatorial ligands on the axial and rhombic ZFS parameters D and E/D for model compounds $[M(NH_3)_2(NCH)_3(H_2O)_2]^{2+}$ (M = Fe^{II}, Co^{II} and Ni^{II}) calculated at the CASSCF/DCD-CAS(2) level of theory.

Evidently, there is a small impact on the ZFS parameters in the Fe^{II} complexes, and a relatively small and positive D prevails, but the axial type of the magnetic anisotropy in the model complex can be achieved by increasing the rhombicity ($E/D \rightarrow 1/3$) by weakening the ligand field in the equatorial plane and strengthening the ligand field in the axial positions. In the case of Co^{II} complexes, D is definitively positive and large, and its value can be increased by weakening the ligand field in both axial and equatorial directions, which also leads to the escalation of E. The model of the Ni^{II} complex provided a very large and negative D value almost in the whole simulation range, which in general makes such complexes good candidates for observing the axial type of the magnetic anisotropy, also taking into the account very small rhombicity. The equatorial ligands show indisputably a larger impact on the value of D, thus weakening of the equatorial ligand field would increase $|D|$ substantially. To summarize, the careful and rational design of macrocyclic ligands and axial pendant arms is crucial to prepare magnetically interesting complex compounds, however, the design of rigid ligands may be necessary to suppress the deformation of the ideal D_{5h} symmetry induced by the Jahn–Teller effect.

Conclusions

A structurally new macrocyclic ligand with two 2-benzimidazolyl pendant arms (**L**) has been synthesized and it provided axially compressed pentagonal bipyramidal Mn^{II}, Fe^{II}, Co^{II} and Ni^{II} complexes with the largest distortion observed for Ni^{II} complex **4** due to the Jahn–Teller effect. The large magnetic anisotropy was confirmed for Fe^{II}, Co^{II} and Ni^{II} complexes **2–4** and Co^{II} complex **3** behaved as a field-induced SMM with a preferential Raman mechanism of relaxation of magnetization. The obtained results were supported by theoretical CASSCF calculations, which very well correspond to the obtained values of magnetic anisotropy. The CASSCF/CAS-DCD(2) based theoretical simulations provided detailed information about the effect of the equatorial and axial ligand field on the magnetic anisotropy in this class of seven-coordinate Fe^{II}, Co^{II} and Ni^{II} complexes. Furthermore, they provide important information on how to tune/increase the magnetic anisotropy in the future: (i) for the Co^{II} complexes the equatorial and axial ligand field should be decreased and the effect of changing each of them is rather equal, (ii) for the Ni^{II} complexes the equatorial field should be decreased while the axial field should be increased, but the effect of the equatorial one is much more pronounced, (iii) for the Fe^{II} complexes, the changes in both ligand fields alter $|D|$ to a lesser extent, but a large variation in the rhombicity E/D is observed. In this respect, a more rigid macrocycle containing five nitrogen donor atoms could be a reasonable proposition to fulfill the above-mentioned requirements for magnetic anisotropy enhancement. Furthermore, the deprotonization of **L** is even possible, so this could be another way to additionally increase the axial ligand field and enhance the magnetic anisotropy at least for Ni^{II} complexes, and to utilize these complexes as building blocks for the synthesis of more complex polymeric coordination compounds.

According to the electrochemical measurements, ligand **L** stabilizes the oxidation state +II in contrast to +I or +III due to its weaker π-acceptor ability in comparison with its pyridine-analogue **L2**. The trend in redox potentials for the $M^{3+/2+}$ couples (M = Mn, Fe, Co and Ni) in the complexes of **L** and **L2** was found to be $E_{1/2}([\mathbf{ML2}]^{3+/2+}) > E_{1/2}([\mathbf{ML}]^{3+/2+}$ for M = Mn and Fe, while it is opposite for $E_{1/2}([\mathbf{CoL2}]^{3+/2+}) < E_{1/2}([\mathbf{CoL}]^{3+/2+}$ and could be related to the different stabilization of the high spin Mn^{III}/Fe^{III} and low spin Co^{III} complexes and the stronger σ-donor/weaker π-acceptor ability of the benzimidazole group.

In conclusion, modification of the macrocycle with two benzimidazolyl moieties has a beneficial effect on the magnetic anisotropy of especially Co^{II} and Ni^{II} complexes and also alters the redox properties of the prepared complexes. But altogether it can be concluded that the tuning of magnetic anisotropy in seven-coordinate pentagonal bipyramidal late-first-row transition metal complexes with macrocyclic ligands modified by pendant arms is a rather complex problem. More factors including not only the strength of the axial ligand field, but also mainly the strength and symmetry of the equatorial ligand field have to be considered with great care during the rational design of new suitable ligands.

Conflicts of interest

The authors declare no competing financial interest.

Acknowledgements

The authors gratefully acknowledge the Ministry of Education, Youth, and Sports of the Czech Republic - National Program of Sustainability (NPU LO1305) and the Czech Science Foundation (GAČR 17-08992S) for the financial support. The authors also acknowledge funding from the ERC under the European Union's Horizon 2020 research and innovation program (GA No. 714850). This work was also supported by the ESF under the project CZ.02.2.69/0.0/0.0/18_070/0009469. The authors also thank Prof. Z. Trávníček for initial preliminary X-ray diffraction data collection, Dr A. Klanicová for recording IR spectra and Mrs P. Richterová for performing elemental analysis.

References

1 E. L. Gavey and M. Pilkington, *Coord. Chem. Rev.*, 2015, **296**, 125–152.
2 J. Liu, Y.-C. Chen, J.-L. Liu, V. Vieru, L. Ungur, J.-H. Jia, L. F. Chibotaru, Y. Lan, W. Wernsdorfer, S. Gao, X.-M. Chen and M.-L. Tong, *J. Am. Chem. Soc.*, 2016, **138**, 5441–5450.
3 Y.-S. Ding, N. F. Chilton, R. E. P. Winpenny and Y.-Z. Zheng, *Angew. Chem., Int. Ed.*, 2016, **55**, 16071–16074.
4 Y.-C. Chen, J.-L. Liu, L. Ungur, J. Liu, Q.-W. Li, L.-F. Wang, Z.-P. Ni, L. F. Chibotaru, X.-M. Chen and M.-L. Tong, *J. Am. Chem. Soc.*, 2016, **138**, 2829–2837.
5 Z. Zhu, M. Guo, X.-L. Li and J. Tang, *Coord. Chem. Rev.*, 2019, **378**, 350–364.
6 A. K. Bar, P. Kalita, J. P. Sutter and V. Chandrasekhar, *Inorg. Chem.*, 2018, **57**, 2398–2401.
7 A. K. Bar, C. Pichon and J.-P. Sutter, *Coord. Chem. Rev.*, 2016, **308**, 346–380.
8 J. Ferrando-Soria, J. Vallejo, M. Castellano, J. Martínez-Lillo, E. Pardo, J. Cano, I. Castro, F. Lloret, R. Ruiz-García and M. Julve, *Coord. Chem. Rev.*, 2017, **339**, 17–103.
9 M. Feng and M. L. Tong, *Chem. – Eur. J.*, 2018, **24**, 1–22.
10 A. K. Bar, C. Pichon, N. Gogoi, C. Duhayon, S. Ramasesha and J.-P. Sutter, *Chem. Commun.*, 2015, **51**, 3616–3619.
11 A. K. Bar, N. Gogoi, C. Pichon, V. M. L. Durga Prasad Goli, M. Thlijeni, C. Duhayon, N. Suaud, N. Guihéry, A.-L. Barra, S. Ramasesha and J.-P. Sutter, *Chem. – Eur. J.*, 2017, **23**, 4380–4396.
12 P. Antal, B. Drahoš, R. Herchel and Z. Trávníček, *Inorg. Chem.*, 2016, **55**, 5957–5972.
13 D. Shao, S. L. Zhang, X. H. Zhao and X. Y. Wang, *Chem. Commun.*, 2015, **51**, 4360–4363.
14 D. Shao, X.-H. Zhao, S.-L. Zhang, D.-Q. Wu, X.-Q. Wei and X.-Y. Wang, *Inorg. Chem. Front.*, 2015, **2**, 846–853.
15 B. Drahoš, R. Herchel and Z. Trávníček, *Inorg. Chem.*, 2018, **57**, 12718–12726.
16 C. Pichon, N. Suaud, C. Duhayon, N. Guihery and J. P. Sutter, *J. Am. Chem. Soc.*, 2018, **140**, 7698–7704.
17 R. Ruamps, L. J. Batchelor, R. Maurice, N. Gogoi, P. Jiménez-Lozano, N. Guihéry, C. de Graaf, A.-L. Barra, J.-P. Sutter and T. Mallah, *Chem. – Eur. J.*, 2013, **19**, 950–956.
18 X.-C. Huang, C. Zhou, D. Shao and X.-Y. Wang, *Inorg. Chem.*, 2014, **53**, 12671–12673.
19 D. Shao, S. L. Zhang, L. Shi, Y. Q. Zhang and X. Y. Wang, *Inorg. Chem.*, 2016, **55**, 10859–10869.
20 D. Shao, L. Shi, S.-L. Zhang, X.-H. Zhao, D.-Q. Wu, X.-Q. Wei and X.-Y. Wang, *CrystEngComm*, 2016, **18**, 4150–4157.
21 B. Drahoš, R. Herchel and Z. Trávníček, *Inorg. Chem.*, 2017, **56**, 5076–5088.
22 A. K. Mondal, A. Mondal, B. Dey and S. Konar, *Inorg. Chem.*, 2018, **57**, 9999–10008.
23 N. Gogoi, M. Thlijeni, C. Duhayon and J.-P. Sutter, *Inorg. Chem.*, 2013, **52**, 2283–2285.
24 V. S. Mironov, T. A. Bazhenova, Y. V. Manakin, K. A. Lyssenko, A. D. Talantsev and E. B. Yagubskii, *Dalton Trans.*, 2017, **46**, 14083–14087.
25 Y. V. Manakin, V. S. Mironov, T. A. Bazhenova, K. A. Lyssenko, I. F. Gilmutdinov, K. S. Bikbaev, A. A. Masitov and E. B. Yagubskii, *Chem. Commun.*, 2018, **54**, 10084–10087.
26 R. Boča, Zero-field splitting in metal complexes, *Coord. Chem. Rev.*, 2004, **248**, 757–815.
27 D. Gatteshi, R. Sessoli and J. Villain, *Molecular Nanomegnets*, Oxford University Press, New York, 2006.
28 Molecular Nanomagnets and Related Phenomena, in *Structure and Bonding*, ed. S. Gao, Springer, Berlin, 2015, vol. 164.

29 J. S. Miller and D. Gatteschi, Molecule-based magnets themed issue No. 6, *Chem. Soc. Rev.*, 2011, **40**, 3065–3365.
30 C. A. P. Goodwin, F. Ortu, D. Reta, N. F. Chilton and D. P. Mills, *Nature*, 2017, **548**, 439–441.
31 F.-S. Guo, B. M. Day, Y.-C. Chen, M.-L. Tong, A. Mansikkamäki and R. A. Layfield, *Science*, 2018, **362**, 1400–1403.
32 M. Atanasov, D. Aravena, E. Suturina, E. Bill, D. Maganas and F. Neese, *Coord. Chem. Rev.*, 2015, **289–290**, 177–214.
33 V. A. Kopotkov, D. V. Korchagin, V. D. Sasnovskaya, I. F. Gilmutdinov and E. B. Yagubskii, *Magnetochemistry*, 2019, **5**, 58.
34 B. Drahoš, R. Herchel and Z. Trávníček, *RSC Adv.*, 2016, **6**, 34674–34684.
35 C. Platas-Iglesias, L. Vaiana, D. Esteban-Gómez, F. Avecilla, J. A. Real, A. de Blas and T. Rodríguez-Blas, *Inorg. Chem.*, 2005, **44**, 9704–9713.
36 L. Vaiana, M. Regueiro-Figueroa, M. Mato-Iglesias, C. Platas-Iglesias, D. Esteban-Gómez, A. de Blas and T. Rodríguez-Blas, *Inorg. Chem.*, 2007, **46**, 8271–8282.
37 P. Antal, B. Drahoš, R. Herchel and Z. Trávníček, *Dalton Trans.*, 2016, **45**, 15114–15121.
38 P. Antal, B. Drahoš, R. Herchel and Z. Trávníček, *Eur. J. Inorg. Chem.*, 2018, **2018**, 4286–4297.
39 I. Nemec, R. Herchel, I. Svoboda, R. Boca and Z. Travnicek, *Dalton Trans.*, 2015, **44**, 9551–9560.
40 X. Xiaoming, M.-a. Haga, T. Matsumura-Inoue, Y. Ru, A. W. Addison and K. Kano, *J. Chem. Soc., Dalton Trans.*, 1993, **16**, 2477–2484.
41 M. Boča, R. F. Jameson and W. Linert, *Coord. Chem. Rev.*, 2011, **255**, 290–317.
42 Q.-X. Li, Q.-H. Luo, Y.-Z. Li, C.-Y. Duan and Q.-Y. Tu, *Inorg. Chim. Acta*, 2005, **358**, 504–512.
43 A. Rodríguez-Rodríguez, I. Carreira-Barral, D. Esteban-Gómez, C. Platas-Iglesias, A. de Blas and T. Rodríguez-Blas, *Inorg. Chim. Acta*, 2014, **417**, 155–162.
44 A. El Majzoub, C. Cadiou, I. Déchamps-Olivier, F. Chuburu and M. Aplincourt, *Eur. J. Inorg. Chem.*, 2007, **32**, 5087–5097.
45 A. E. Majzoub, C. Cadiou, I. Déchamps-Olivier, F. Chuburu, M. Aplincourt and B. Tinant, *Inorg. Chim. Acta*, 2009, **362**, 1169–1178.
46 M. Regueiro-Figueroa, D. Esteban-Gómez, C. Platas-Iglesias, A. de Blas and T. Rodríguez-Blas, *Eur. J. Inorg. Chem.*, 2007, **15**, 2198–2207.
47 A. El Majzoub, C. Cadiou, I. Dechamps-Olivier, B. Tinant and F. Chuburu, *Inorg. Chem.*, 2011, **50**, 4029–4038.
48 C. M. Fisher, E. Fuller, B. P. Burke, V. Mogilireddy, S. J. Pope, A. E. Sparke, I. Dechamps-Olivier, C. Cadiou, F. Chuburu, S. Faulkner and S. J. Archibald, *Dalton Trans.*, 2014, **43**, 9567–9578.
49 B. Drahoš, J. Kotek, P. Hermann, I. Lukeš and E. Tóth, *Inorg. Chem.*, 2010, **49**, 3224–3238.
50 J. Prousek, *Collect. Czech. Chem. Commun.*, 1991, **56**, 1358–1360.
51 S. Stoll and A. Schweiger, *J. Magn. Reson.*, 2006, **178**, 42–55.
52 MATLAB, The Mathworks Inc., Natick, MA, USA.
53 V. V. Pavlishchuk and A. W. Addison, *Inorg. Chim. Acta*, 2000, **298**, 97–102.
54 G. M. Sheldrick, *Acta Crystallogr., Sect. C: Struct. Chem.*, 2015, **71**, 3–8.
55 A. L. Spek, *Acta Crystallogr., Sect. D: Biol. Crystallogr.*, 2009, **65**, 148–155.
56 C. F. Macrae, I. J. Bruno, J. A. Chisholm, P. R. Edgington, P. McCabe, E. Pidcock, L. Rodriguez-Monge, R. Taylor, J. van de Streek and P. A. Wood, *J. Appl. Crystallogr.*, 2008, **41**, 466–470.
57 F. Neese, *Wiley Interdiscip. Rev.: Comput. Mol. Sci.*, 2012, **2**, 73–78.
58 F. Neese, *Wiley Interdiscip. Rev.: Comput. Mol. Sci.*, 2018, **8**, e1327.
59 P. A. Malmqvist and B. O. Roos, *Chem. Phys. Lett.*, 1989, **155**, 189–194.
60 C. Angeli, R. Cimiraglia and J.-P. Malrieu, *Chem. Phys. Lett.*, 2001, **350**, 297–305.
61 C. Angeli, R. Cimiraglia, S. Evangelisti, T. Leininger and J.-P. Malrieu, *J. Chem. Phys.*, 2001, **114**, 10252–10264.
62 C. Angeli, R. Cimiraglia and J.-P. Malrieu, *J. Chem. Phys.*, 2002, **117**, 9138–9153.
63 F. Weigend and R. Ahlrichs, *Phys. Chem. Chem. Phys.*, 2005, **7**, 3297–3305.
64 D. Ganyushin and F. Neese, *J. Chem. Phys.*, 2006, **125**, 024103.
65 F. Neese, *J. Chem. Phys.*, 2005, **122**, 034107.
66 R. Maurice, R. Bastardis, C. de Graaf, N. Suaud, T. Mallah and N. Guihéry, *J. Chem. Theory Comput.*, 2009, **5**, 2977–2984.
67 F. Weigend, *Phys. Chem. Chem. Phys.*, 2006, **8**, 1057–1065.
68 A. Hellweg, C. Hättig, S. Höfener and W. Klopper, *Theor. Chem. Acc.*, 2007, **117**, 587–597.
69 S. Pathak, L. Lang and F. Neese, *J. Chem. Phys.*, 2017, **147**, 234109.
70 K. Momma and F. Izumi, *J. Appl. Crystallogr.*, 2011, **44**, 1272–1276.
71 M. Regueiro-Figueroa, L. M. Lima, V. Blanco, D. Esteban-Gomez, A. de Blas, T. Rodriguez-Blas, R. Delgado and C. Platas-Iglesias, *Inorg. Chem.*, 2014, **53**, 12859–12869.
72 B. Drahoš, R. Herchel and Z. Trávníček, *Inorg. Chem.*, 2015, **54**, 3352–3369.
73 S. Alvarez, *Dalton Trans.*, 2005, **13**, 2209–2233.
74 D. Casanova, P. Alemany, J. M. Bofill and S. Alvarez, *Chem. – Eur. J.*, 2003, **9**, 1281–1295.
75 R. Boča, *Theoretical Foundations of Molecular Magnetism*, Elsevier, Amsterdam, 1999.
76 The standard deviations were calculated as $\sigma_i = (P_{ii}^{-1} \cdot S/(N-k))^{-1/2}$, where $P_{ij} = \Sigma(\delta\mu_n/\delta a_i \cdot \delta\mu_n/\delta a_j)$ and $S = \Sigma(\mu_n - \mu_n^{exp})^2$ with $n = 1$ to N; a_i and a_j are fitted parameters, N is the number of experimental points (the sum of temperature and field dependent data), μ_n and μ_n^{exp} are the calculated and experimental effective magnetic moments for a given temperature and magnetic field. The σ_i was then mul-

tiplied by Student's $t_{95\%}$ to provide confidence limits with 95% probabilities listed in the text.

77 S. Gomez-Coca, A. Urtizberea, E. Cremades, P. J. Alonso, A. Camon, E. Ruiz and F. Luis, *Nat. Commun.*, 2014, **5**, 1–8.

78 L. Chen, S.-Y. Chen, Y.-C. Sun, Y.-M. Guo, L. Yu, X.-T. Chen, Z. Wang, Z. W. Ouyang, Y. Song and Z.-L. Xue, *Dalton Trans.*, 2015, **44**, 11482–11490.

79 Y.-F. Deng, B. Yao, P.-Z. Zhan, D. Gan, Y.-Z. Zhang and K. R. Dunbar, *Dalton Trans.*, 2019, **48**, 3243–3248.

80 Mn^{II}, Fe^{II} and Co^{II} complexes of **L2** were resynthesized according to ref. 12 and the $E_{1/2}$ values were remeasured. The obtained data are in very good agreement with the previously published data in ref. 12 if these data were recalculated using the new value $E_{1/2}$ = 0.624 V *vs.* SHE for ferrocene/ferrocenium standard and its potential $E_{1/2}$ = 0.075 V *vs.* Ag/Ag^{+} during the measurement.

81 M. Atanasov, D. Ganyushin, K. Sivalingam and F. Neese, in *Molecular Electronic Structures of Transition Metal Complexes II*, ed. D. M. P. Mingos, P. Day and J. P. Dahl, Springer, Berlin, Heidelberg, 2012, pp. 149–220.

82 S. K. Singh, J. Eng, M. Atanasov and F. Neese, *Coord. Chem. Rev.*, 2017, **344**, 2–25.